How to Promote Earthquake Ruptures: Different Nucleation Strategies in a Dynamic Model with Slip-Weakening Friction

by Andrea Bizzarri

Abstract The introduction of the linear slip-weakening friction law permits the solution of the elastodynamic equation for a rupture that develops on a fault by removing the singularity in the components of stress tensor, thereby ensuring a finite energy flux at the crack tip. With this governing model, largely used by seismologists, it is possible to simulate a single earthquake event; but, in the absence of remote tectonic loading, it requires the introduction of an artificial procedure to initiate the rupture (i.e., to reach the failure stress point). In this article, by studying the dynamic rupture propagation and the solutions on the fault and on the free surface, I systematically compare three conceptually and algorithmically different nucleation strategies widely adopted in the literature: the imposition of an initially constant rupture speed, the introduction of a shear stress asperity, and the perturbation to the initial particle velocity field. My results show that, contrary to supershear ruptures, which tend to forget their origins, subshear ruptures are quite sensitive to the adopted nucleation procedure, which can bias the runaway rupture. I confirm that the most gradual transition from imposed nucleation and spontaneous propagation is obtained by initially forcing the rupture to expand at a properly chosen, constant speed (0.75 times the Rayleigh speed). I also numerically demonstrate that a valid alternative to this strategy is an appropriately smoothed, elliptical shear stress asperity. Moreover, I evaluate the optimal size of the nucleation patch where the procedure is applied; the simulations indicate that its size has to equal the critical distance of Day (1982) in the case of supershear ruptures and to exceed it in the case of subshear ruptures.

Introduction

Overview

A large quantity of information about physical processes occurring during an earthquake event can be inferred from the results of dynamic models of seismic sources. In these mixed boundary condition problems, the slip is assigned outside the region experiencing the rupture (typically assumed at rest or in a stable sliding regime), and the traction components are assigned inside this region. The rupture occurrence at a point on the surface (or in the volumetric region) of discontinuity of the medium (the fault) is determined by a fracture criterion, expressed in terms of maximum frictional resistance or in terms of energy. The singularities (in components of stress tensor and energy) at the tip of the rupture are removed by the introduction of a governing law which relates the magnitude of traction on the fault surface to some physical observables, such as the slip, the slip velocity, etc. This makes it possible to obtain a nonsingular solution of the elastodynamic equation in a discontinuous medium.

In the recent literature, there is a lively debate about the most reasonable and realistic (from a physical point of view) analytical formulation of a fault governing law (Bizzarri and Cocco, 2006; Rice and Cocco, 2007) and the issue is still open (Bizzarri, 2010). The most widely adopted (see for instance Harris *et al.*, 2009) constitutive model is the slip-weakening (SW) law, which prescribes that the magnitude τ of fault traction decreases for increasing cumulative fault slip (Ida, 1972). The SW law, motivated by the cohesive zone models developed for tensile fractures by Dugdale (1960), Barenblatt (1962), and Bilby *et al.* (1963), is conceptually simple, and its incorporation within the numerical codes is straightforward compared to other more elaborated friction laws, such as rate-dependent and state-dependent friction laws (e.g., Dieterich, 1979). Moreover, it contains perhaps the most physically reasonable feature of a constitutive model, that the stress on the fault decreases (due to abrasion of surface asperities) as the rupture propagates and the fault slip accumulates. This attribute has been clearly recognized (Cocco and Bizzarri, 2002) also in the laboratory-derived rate- and state-dependent friction laws.

Contrary to rate- and state-dependent friction laws, by assuming the linear SW law, it is impossible to simulate repeated ruptures on the same fault (i.e., to model the whole

seismic cycle); and, more interestingly for the present matter, it is impossible to numerically reproduce the spontaneous rupture nucleation unless external, time variable loading is inserted in the model (e.g., the tectonic load). As a matter of fact, the linear SW law does not contain any hardening effect (i.e., the strength increase for increasing slip; see for instance Matsu'ura *et al.*, 1992), and it prescribes that the fault remains locked into its initial equilibrium state until the static level of friction is reached. Therefore, the fault friction has to be increased, in some way, from the initial value (τ_0, the stress distribution prior to the rupture) up to the static level. Evidently, in the specific case of a single dynamic rupture controlled by a linear SW law, the artificial increase of fault friction previously described is not a physical but rather a purely numerical procedure necessary to produce the desired rupture, which expands on the fault in a dynamic fashion. Obviously, the dynamic models resulting from the application of this procedure have to satisfy some criteria, which will be described in the Quantitative Criteria for the Evaluation of the Nucleation Strategy section.

Critical Lengths for Nucleation

Two of the crucial aspects of the introduction of the artificial nucleation are the size and the shape of the fault patch where the nucleation procedure is applied. In the remainder of this article, I will use I_{nucl} to denote this region, named the initialization (or nucleation) area, having border $\partial I_{\mathrm{nucl}}$ (Fig. 1). In the literature, several critical lengths have been introduced to quantify the size of I_{nucl}; in this article, I will
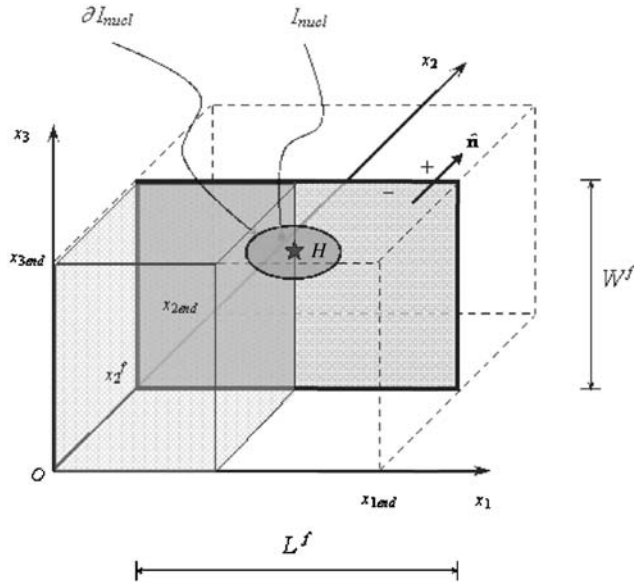
Figure 1. Geometry of the considered seismogenic model. The star denotes the imposed hypocenter H and I_{nucl} is the initialization zone, with border $\partial I_{\mathrm{nucl}}$. The light gray plane indicates the fault $x_2 = x_2^f$, oriented through its normal unit vector $\hat{n}$ and having aspect ratio L^f/W^f. The dotted gray box marks the portion of the computational domain where calculations are performed, due to the exploitation of the symmetry about H and about the fault plane.

quantify the dimensions of I_{nucl} by referring to these quantities and to their mutual relationships.

Starting from energy balance considerations, Andrews (1976b) analytically derived an expression for the half-length that a 2D, purely inplane (i.e., mode II), bilateral crack has to reach in order to be able to spontaneously propagate farther:

$$L_c^{(\mathrm{II})} = \frac{2}{\pi} G \frac{\lambda + G}{\lambda + 2G} \frac{\tau_u - \tau_f}{(\tau_0 - \tau_f)^2} d_0. \qquad (1)$$

Equation (1) has its counterpart in the case of a 2D, purely antiplane (i.e., mode III), bilateral crack (Andrews, 1976a):

$$L_c^{(\mathrm{III})} = \frac{G}{\pi} \frac{\tau_u - \tau_f}{(\tau_0 - \tau_f)^2} d_0. \qquad (2)$$

In equations (1) and (2), λ and G are the Lamé constants; τ_u (which equals $\mu_u \sigma_n^{\mathrm{eff}}$) is the static stress in the SW model (where σ_n^{eff} is the effective normal stress); τ_f (which equals $\mu_f \sigma_n^{\mathrm{eff}}$) is the kinetic level of traction; and d_0 is the characteristic SW distance (defining the breakdown—or cohesive—zone, where the stress drop is realized).

By considering an initially circular, uniformly expanding 3D crack and by balancing the strain energy release rate and the energy dissipation rate at the crack edge, Day (1982) estimated the critical fundamental length scale for the dynamic solution as:

$$r_c^{(D)} = \frac{7\pi}{24} G \frac{\tau_u - \tau_f}{(\tau_0 - \tau_f)^2} d_0, \qquad (3)$$

which, for a Poissonian medium (i.e., when $\lambda = G$), is systematically greater (for the same parameters) than $L_c^{(\mathrm{II})}$. Because of its theoretical derivation, the length scale defined in equation (3) appear to be appropriate to my fault model (see the Fault Model and Numerical Method section). Even if the dynamics of some large strike-slip earthquakes can be understood by considering them as mode II ruptures (because they are dominated by the inplane sliding), in general it is well known that 3D problems are not simply a combination of modes II and III (e.g., Bizzarri and Cocco, 2005). In the following sections of this article, I also will consider the critical length scales defined by equations (1) and (2) because there are some attempts to quantify the extension of the initialization zone in 3D geometries in terms of $L_c^{(\mathrm{II})}$ and $L_c^{(\mathrm{III})}$.

Uenishi and Rice (2004) generalized the case of an infinite, homogeneous, elastic space from the 2D analysis made by Uenishi and Rice (2003) to a 3D geometry and analytically found universal nucleation lengths for fault instability, which are the major and minor semi-axes of an elliptical initialization zone. In the case of Poisson's ratio $\nu = 0.25$, they are expressed as

$$a_c^{(\mathrm{UR})} \cong 1.299 G \frac{d_0}{\tau_u - \tau_f} \qquad (4)$$

and

$$b_c^{(UR)} \cong 0.9755 G \frac{d_0}{\tau_u - \tau_f}, \qquad (5)$$

respectively. Interestingly, the ratio $a_c^{(UR)}/b_c^{(UR)} = 1.33$ equals the ratio $L_c^{(II)}/L_c^{(III)}$ for a Poissonian medium. When these critical nucleation lengths are reached, the quasi-static regime no longer exists; the instability is then dynamically controlled by the friction law, and the rupture grows spontaneously. Contrary to the other critical lengths, $a_c^{(UR)}$ and $b_c^{(UR)}$ are independent on the prestress τ_0. The Uenishi and Rice (2004) model additionally includes a condition specifying the shape of slip and traction; in this article, I will not directly compare my results with the Uenishi and Rice model but will simply consider the critical lengths defined in equations (4) and (5) when evaluating the size of I_{nucl}.

Finally, for a Poissonian medium, note that if $(1 + S)^2 > 3.06$ (where $S \underset{df}{=} \frac{\tau_u - \tau_0}{\tau_0 - \tau_f}$ is the strength parameter; Andrews, 1976b), it results in $a_c^{(UR)} < L_c^{(II)} < r_c^{(D)}$ and $b_c^{(UR)} < L_c^{(III)} < r_c^{(D)}$.

Goals of the Present Study

The study of the nucleation process is an extremely challenging problem from a numerical point of view (see Lapusta et al., 2000, for a discussion), and the efforts spent are motivated by several reasons. First, nucleation has a fundamental importance in the physics of earthquakes *per se*. Second, it has immediate practical implications (e.g., Iio, 1995; Lapusta and Rice, 2003). Finally, because the relation between strength of its initiation (i.e., the nucleation size) and the ultimate size of the ensuing earthquake event has been the matter of an animated debate (Ellsworth and Beroza, 1995; Kilb and Gomberg, 1999).

A detailed study of the nucleation process that accounts for the underlying physics (describing the evolution of slip on a pre-existing main frictional surface or in an increasing coalescence of distributed microcracks in a rock volume, solicited by progressive loading) is beyond the purposes of the present paper. (For some connections between nucleation phase and properties of a dynamic rupture, see Festa and Villotte [2006] and Shi and Ben–Zion [2006].) On the contrary, the aim of the present study is to provide a methodological tutorial on algorithmic issues associated with the problem of the initiation of a synthetic rupture. I emphasize that without a systematic comparison of the different nucleation strategies it is impossible to establish *a priori* how much the resulting rupture propagation is biased by the nucleation procedure and what optimal parameters should be used (size and shape of initialization patch, inherent parameters of each nucleation algorithm).

As will be discussed in the Different Nucleation Strategies section, different nucleation strategies have been used in the various implementation of SW law presented in the literature (Day, 1982; Andrews, 1985; Ionescu and Campillo, 1999; Bizzarri and Cocco, 2005; and Dunham and Bhat, 2008, among many others), but they have not been rigorously and systematically compared. This article aims to fill this gap.

The scientific objectives of the present paper can be summarized as follows: (1) to explore and quantify, through numerical experiments representative of typical crustal earthquakes, the effects of the different nucleation procedures on the further rupture propagation and on the synthetic signals on the free surface; and (2) to try to establish the parameters that have to be used in the various strategies to obtain the desired solution of the dynamic problem. In the comparison of the results of the numerical experiments I will rely on the quantitative criteria described in the Quantitative Criteria for the Evaluation of the Nucleation Strategy section.

Fault Model and Numerical Method

In this article, I consider an isolated, planar, strike-slip fault embedded in a perfectly elastic, isotropic half–space, initially at rest and subjected only to stress perturbations excited by the earthquake source. The considered fault geometry is reported in Figure 1. The elastodynamic problem is numerically solved by neglecting body forces, by using the conventional grid, finite difference code described in Bizzarri and Cocco (2005), which is second-order accurate in space and in time and is OpenMP parallelized. The rupture developing on the fault is fully dynamic because I include full account of inertial effects (see also Bizzarri and Belardinelli, 2008) and is truly 3D because the equations of motion are solved independently for both the components of physical observables, allowing rake rotation. Each component of the solutions (slip, slip velocity, and traction) depends on both of the two on–fault spatial coordinates (x_1 and x_3) and on time (t). Because identical material properties on both sides of the fault plane are considered, I exploit the existing symmetries in order to reduce computational effort, as described in detail in Bizzarri (2009a).

The fault is subjected to the linear SW governing law in the following form (Ida, 1972):

$$\tau = \begin{cases} \tau_u - (\tau_u - \tau_f)\frac{u}{d_0} & , u < d_0 \\ \tau_f & , u \ge d_0 \end{cases}, \qquad (6)$$

where u is the magnitude of the fault slip. In the interest of simplicity, I neglect here the possible changes in pore fluid pressure, p_{fluid}; moreover, uniform material properties guarantee a constant value of the normal stress of tectonic origin, σ_n, and therefore $\sigma_n^{eff} (= \sigma_n - p_{fluid})$ also is constant through time.

Different Nucleation Strategies

As previously pointed out, in the case of linear SW law and in absence of tectonic load or stress perturbations coming from other neighboring faults, the nucleation procedure is a numerical artifact needed to induce the rupture to spon-

taneously propagate; that is, to enlarge without prior assigned rupture velocity (v_r is itself a solution of the problem and, depending on fault rheology, it can potentially assume a very complicated distribution; see, for instance, figure 11e in Bizzarri and Spudich, 2008). In all the numerical experiments presented and discussed in the remainder of this article, the earthquake hypocenter H (see Fig. 1) is imposed (it is located in (x_1^H, x_2^f, x_3^H), and it is in the center of the initialization zone I_{nucl}. In the next three subsections, I will describe the various nucleation strategies considered in this study, schematically illustrated in Figure 2.

Initially Nonspontaneous Rupture Propagation

I assume that the rupture is initially nonspontaneous, in that it propagates with a constant rupture velocity, $v_r = v_{\text{force}}$, as in Andrews (1985). Namely, the fault friction is specified as follows (see Fig. 2a):

$$\tau = \begin{cases} \tau_{\text{nucl}} = \min\{\tau^{(\text{SW})}, \tau^{(\text{TW})}\} & , \forall (x_1, x_3) \in I_{\text{nucl}} \\ \tau^{(\text{SW})} & , \forall (x_1, x_3) \notin I_{\text{nucl}} \end{cases}, \quad (7)$$

where $\tau^{(\text{SW})}$ is expressed as in equation (6) and $\tau^{(\text{TW})}$, given by (Bizzarri et al., 2001), is

$$\tau^{(\text{TW})} = \begin{cases} \left[\mu_u - (\mu_u - \mu_f)\frac{(t-t_{\text{force}})}{t_0}\right]\sigma_n^{\text{eff}} & , t - t_{\text{force}} < t_0 \\ \mu_f \sigma_n^{\text{eff}} & , t - t_{\text{force}} \geq t_0 \end{cases}. \quad (8)$$

Formally, equation (8) can be regarded as a constitutive model, the linear time-weakening (TW) law, in which the fault friction explicitly depends on time, instead of on slip, as in the SW model. In equation (8), $t_{\text{force}} = \frac{\sqrt{(x_1 - x_1^H)^2 + (x_3 - x_3^H)^2}}{v_{\text{force}}}$ is the instant of time at which a rupture propagating at the forcing velocity v_{force} reaches the point (x_1, x_3), and t_0 is a characteristic time (the temporal counterpart of d_0). At a certain time (which depends on the adopted frictional parameters), the SW law takes over, and then the rupture begins to propagate spontaneously. To briefly illustrate this strategy, let us consider, for the sake of simplicity, the hypocenter H; here, at $t = 0$, the fault traction has magnitude τ_0, and fault strength is defined by $\tau^{(\text{TW})}$ and equals τ_u (because $u = 0$). Then the fault strength diminishes linearly through time, accordingly to the $\tau^{(\text{TW})}$ function in equation (8). When it reaches τ_0, the sliding begins, and it causes a stress redistribution in the surrounding fault points, which are loaded. This load can be such that the upper-yield stress
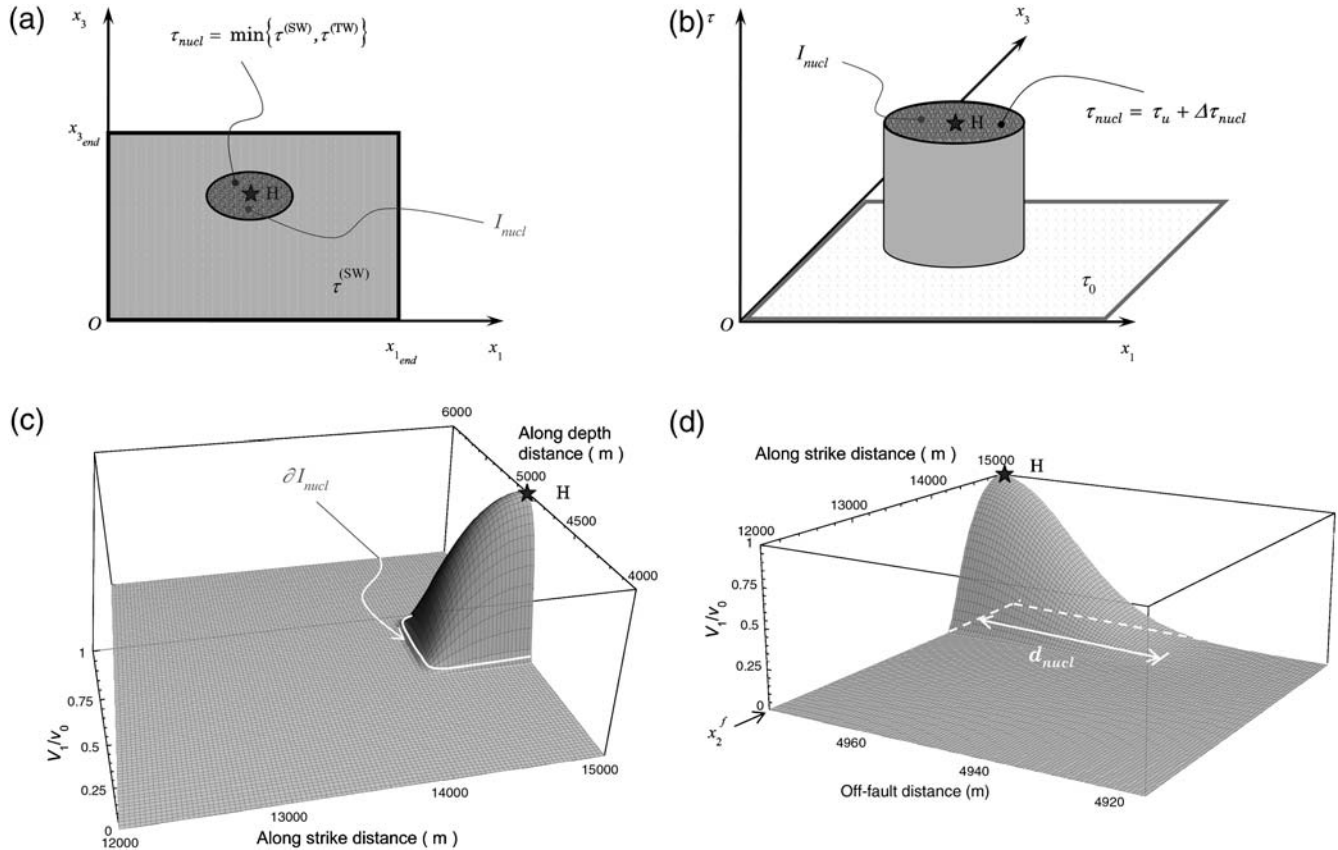
Figure 2. Schematic representation of the three nucleation strategies compared in this article. (a) Initially TW-driven rupture (see Initially Nonspontaneous Rupture Propagation section). (b) Initial shear stress asperity (see Introduction of an Initial Shear Stress Asperity section). (c) and (d) Perturbation to the initial particle velocity (see Perturbation to the Initial Particle Velocity section); (c) V_1/v_0 as a function of on-fault coordinates; (d) V_1/v_0 as a function of x_1 and x_2. In all panels, the imposed hypocenter and the initialization zone are indicated.

τ_u is reached, and therefore these points also start to slip. The additional parameters that come into the model as a consequence of the implementation of this nucleation strategy are v_{force} and t_0.

Introduction of an Initial Shear Stress Asperity

Starting from the hypothesis of Benioff (1951) and Reid (1910) that a fracture occurs when the stress in a volume reaches the rock strength and from the concept of asperity in the sense of Kanamori (1981), it is physically reasonable to assume that, within a region close to the hypocenter, the shear stress is higher than in the remaining portions of the fault and that here the rupture is prone to start to propagate. In accordance to its conceptual simplicity, the numerical implementation of this nucleation strategy is rather trivial; at $t = 0$, the fault traction is (see Fig. 2b)

$$\tau = \begin{cases} \tau_{\text{nucl}} = \tau_u + \Delta\tau_{\text{nucl}} & , \forall \ (x_1, x_3) \in I_{\text{nucl}} \\ \tau_0 & , \forall \ (x_1, x_3) \notin I_{\text{nucl}} \end{cases}, \quad (9)$$

where $\Delta\tau_{\text{nucl}}$, the additional parameter inserted into the model by the introduction of this nucleation strategy, is a (small) perturbation to τ_u (namely it is a static overshoot). In the remainder of this article (see Results for Subshear Rupture Propagation), I will discuss a possible refinement in this strategy, consisting of tapering τ_{nucl} from $\tau_u + \Delta\tau_{\text{nucl}}$ to τ_0 over a finite distance instead of having an abrupt transition between $\tau_u + \Delta\tau_{\text{nucl}}$ and τ_0 at ∂I_{nucl}.

Perturbation to the Initial Particle Velocity

It is well known that stress redistribution following an earthquake corresponds to a propagation of seismic waves in the medium surrounding the earthquake source (e.g., Bizzarri and Belardinelli, 2008, among many others). This wave excitation causes perturbations of the particle velocity in the medium that can lead to dynamic triggering, which in some situations can even be relatively abrupt. Starting from this physical basis, the third type of artificial nucleation I consider assumes that, in a volume surrounding the imposed hypocenter, the particle velocity $\mathbf{V}$ is non-null. Formally, following Ionescu and Campillo (1999) and Badea *et al.* (2004) with appropriate modifications, I prescribe that at $t = 0$ the components of $\mathbf{V}$ are expressed as

$$V \begin{Bmatrix} 1 \\ 2 \\ 3 \end{Bmatrix} (x_1, x_2, x_3, 0)$$

$$= \frac{1}{2}\text{sign}\left(x_2 - x_2^f\right) v_0 \begin{Bmatrix} \cos\varphi \\ 0 \\ \sin\varphi \end{Bmatrix} e^{\frac{(x_1 - x_1^H)^2}{(x_1 - x_1^H)^2 - l_1^2}} e^{\frac{(x_3 - x_3^H)^2}{(x_3 - x_3^H)^2 - l_2^2}} e^{\frac{(x_2 - x_2^f)^2}{(d_{\text{nucl}})^2}}$$

$$\times \Theta(l_1^2 - (x_1 - x_1^H)^2)\Theta(l_2^2 - (x_3 - x_3^H)^2), \quad (10)$$

where v_0 is the modulus of the initial fault slip velocity in H; φ is the rake angle; l_1 and l_2 parameterize I_{nucl} in the x_1 and x_3 direction, respectively; d_{nucl} is a sensitivity factor, controlling how rapidly the perturbation to V_i decreases to the reference value of 0 while moving in the direction perpendicular to the fault plane $x_2 = x_2^f$ (see Fig. 2d; because the medium is initially at rest, $\mathbf{V} = 0$ is the reference state of the elastic medium), and $\Theta(.)$ is the Heaviside function. In the framework of the traction-at-split-nodes numerical technique (see Bizzarri and Cocco, 2005, and references therein for further details), the components of the initial fault slip velocity are expressed as

$$v_i(x_1, x_3, 0) = V_i^+(x_1, x_3, 0) - V_i^-(x_1, x_3, 0),$$

where $V_i^+(x_1, x_3, 0)$ and $V_i^-(x_1, x_3, 0)$ are the components of $\mathbf{V}$ in the positive and negative parts of the medium separated by the fault, respectively (see Fig. 1), and $i = 1, 2, 3$. From equation (10), I have that, in H,

$$V_1^+(x_1^H, x_3^H, 0) - V_1^-(x_1^H, x_3^H, 0) = v_0 \cos\varphi,$$

$$V_2^+(x_1^H, x_3^H, 0) - V_2^-(x_1^H, x_3^H, 0) = 0, \quad \text{and}$$

$$V_3^+(x_1^H, x_3^H, 0) - V_3^-(x_1^H, x_3^H, 0) = v_0 \sin\varphi,$$

in agreement with the formal definition of v_0. This nucleation strategy causes fault points within I_{nucl} to move at $t = 0$ with a velocity that is maximum in H (where it is v_0, as previously noticed) and is exponentially tapered to 0 at the border ∂I_{nucl} (see Fig. 2c). The difference between V_i^+ and V_i^- induces a differential force between the split nodes, which in turn will cause a differential acceleration, ultimately leading to a readjustment in the fault traction. When a fault point is slipping, the fault friction is then determined by the governing law (equation (6)). The basic difference of this nucleation strategy with respect to those described in the Initially Nonspontaneous Rupture Propagation and Introduction of an Initial Shear Stress Asperity subsections is that the previous strategies change the reference state of the variables only on the fault plane (fault strength and prestress, respectively), while the current strategy introduces a modification in $\mathbf{V}$ in a volume surrounding the hypocenter. The additional parameters inserted into the model with this nucleation strategy are d_{nucl} and v_0.

Quantitative Criteria for the Evaluation of the Nucleation Strategy

Because the spontaneous, fully dynamic rupture problem does not have a closed-form analytical solution (even in homogeneous conditions), there is no theoretical solution of the problem that can be taken as a reference against which to compare the different solutions obtained numerically by adopting the various nucleation strategies. In the evaluation

of the solutions obtained with different nucleation strategies, I will consider the following criteria that have to be satisfied.

1. As previously noted, the inertia is always considered (i.e., I do not use the quasi-static approximation to solve the elastodynamic equation).
2. The transition between the early stages of the rupture (primarily controlled by the nucleation strategy) and the further spontaneous dynamic rupture propagation (controlled by the adopted constitutive law) has to be gradual in both space and time, without abrupt discontinuities in rupture velocity, stress drop, etc.
3. The rupture speed of the ongoing dynamic rupture has to satisfy the rules based on the value of the strength parameter (see for instance Dunham, 2007); for example, a low-strength fault (like configuration A described in the Results from Numerical Experiments: Supershear Rupture Propagation section) would accelerate up to supershear speeds, while a high-strength fault (like configuration B in the Results for Subshear Rupture Propagation section) would remain subshear.
4. The extension of the initialization zone has to be as small as possible; and, once nucleated, the rupture has to propagate spontaneously and dynamically outside I_{nucl}.
5. At fault nodes located outside I_{nucl}, the rupture has to reproduce the imposed SW law, with its constitutive parameters.

A solution that better satisfies all these criteria characterizes what I select as the desired solution.

Results from Numerical Experiments: Supershear Rupture Propagation

In this article, I consider a set of parameters that is representative of a typical crustal earthquake occurring at a depth of 5 km. In particular, I adopt the same parameterization of the medium surrounding the fault adopted in Version 3 of the Southern California Earthquake Center (SCEC) benchmark problem (e.g., Harris *et al.*, 2004); the other frictional parameters are listed in Table 1. I consider the idealized situation of homogeneous rheology; that is, frictional heterogeneities on the fault (except for I_{nucl}) are neglected. Of course, this might not represent a realistic assumption for natural faults (e.g., Rivera and Kanamori, 2002), but here I am interested in the effects of the nucleation on the rupture propagation and therefore wanted to disregard any complication arising from a potentially complex fault rheology, such as local transitions to supershear regimes (Liu and Lapusta, 2008; Bizzarri *et al.*, 2010). I consider two different sets of parameters that are representative of two distinct classes of rupture regimes: configuration A is a low-strength fault ($S = 0.4$), which can produce supershear ruptures, while configuration B is a high-strength fault ($S = 2$), where ruptures remain subshear. If not otherwise explicitly mentioned, the parameters of various nucleation strategies are those tabulated in Table 2.

Figure 3a shows the distribution on the fault plane of the rupture times ($t_r(x_1, x_3)$) for the three nucleation procedures described in the Different Nucleation Strategies section. In the case of initial shear asperity, I consider three shapes: a circle (as suggested by the meaning of the critical radius $r_c^{(D)}$ of Day, 1982), an ellipse (as suggested by the two critical lengths $L_c^{(II)}$ and $L_c^{(III)}$ of Andrews, 1976a, and 1976b, as well as by $a_c^{(UR)}$ and $b_c^{(UR)}$ of Uenishi and Rice, 2004), and a square (as in SCEC benchmarks; Harris *et al.*, 2009). The rupture time t_r at a generic fault point is defined as the instant at which the slip velocity at that point exceeds $v_l = 0.01$ m/sec, a threshold value that appropriately captures the initiation of dynamic slip (see Bizzarri and Spudich, 2008 and references therein). I then calculate the rupture velocity ($v_r(x_1, x_3)$) as the inverse of slowness: $v_r(x_1, x_3) = \frac{1}{\|\nabla_{(x_1,x_3)} t_r(x_1,x_3)\|}$. Recall that, in the case of configuration A, the maximum allowable rupture speed (Burridge *et al.*, 1979) is $v_{r_{max}} = v_P$ (where v_P is the P-wave speed), which is in fact attained in my models, and is in accord with previous studies (e.g., Bizzarri and Cocco, 2005; Liu and Lapusta, 2008) and with laboratory experiments (e.g., Xia *et al.*, 2004). In Figure 3b, I superimpose the boundary lines separating the fault points experiencing supershear rupture velocities (points on the left of each line) from those remaining subshear (points on the right of each line). From these two panels, the overall behavior of the rupture is nearly the same; the shapes of the rupture, at a given time level, are similar, and all solutions satisfy all the criteria (1–5) in the Quantitative Criteria for the Evaluation of the Nucleation Strategy section. By looking at the details of each numerical experiment, it emerges that there is a temporal difference in the arrival of rupture front. This delay is also viewable from the time evolutions of the fault slip velocity (Fig. 3c) and those of particle velocity components (Fig. 4). The peaks are nearly the same, even if particle velocity perturbation (magenta curve) produces differences in V_1 (Fig. 4a). The numerical oscillations are practically the same in all models; this indicates that the accuracy of the simulated rupture is primarily controlled by the spatiotemporal discretization and not by the choice of the nucleation procedure.

In all previous simulations the size (radius, major semi-axis, side) of I_{nucl} was the same and equal to $r_c^{(D)}$, a conservative choice. On the other hand, by imposing an elliptical asperity having $r_a = L_c^{(II)}$ and $r_b = L_c^{(III)}$, respectively, the rupture initially starts to propagate, but very rapidly dies (therefore criteria 4 and 5 are not satisfied). This is not surprising, given the fact that $L_c^{(II)}$ and $L_c^{(III)}$ have been theoretically derived for purely 2D problems. The same occurs by setting $r_a = 1.36 L_c^{(II)}$ and $r_b = 1.36 L_c^{(III)}$, respectively; this suggests that the multiplicative factor of 1.36 suggested by Galis *et al.* (2010) for supershear ruptures is not universal but strongly depends on the adopted frictional parameters and in particular is not correct in the case of configuration A. I have extensively explored the parameters' space and found that the minimum value of this multiplicative factor, guaranteeing spontaneous rupture propagation, is 1.45.

Table 1

Model Discretization and Constitutive Parameters Adopted in This Study

Parameter	Value	
	Configuration A	Configuration B
Medium and Discretization Parameters		
Lamé constants, $\lambda = G$	32 GPa	
Rayleigh velocity, v_R	3.184 km/sec	
S-wave velocity, v_S	3.464 km/sec	
Eshelby velocity, $v_E = \sqrt{2}v_S$	4.899 km/sec	
P-wave velocity, v_P	6 km/sec	
Maximum allowed rupture velocity, $v_{r_{max}}$	v_P	v_R
Cubic mass density, ρ	2670 kg/m^3	
Fault length, L^f	30 km[*]	
Fault width, W^f	10 km[*]	
Spatial grid sampling, $\Delta x_1 = \Delta x_2 = \Delta x_3 \equiv \Delta x$	25 m	
Time step, Δt	1.2×10^{-3} sec	
Courant–Friedrichs–Lewy ratio, $\omega_{CFL} = v_S \Delta t / \Delta x$	0.166	
Critical frequency for spatial grid dispersion, $f_{acc}^{(s)} = v_S/(6\Delta x)$	23.1 Hz	
Location of the fault, x_2^f	4.975 km	
Coordinates of the imposed hypocenter, $H \equiv (x_1^H, x_2^f, x_3^H)$	(15,4.975,5) km	
Domain boundary conditions	$x_1 = 0$: ABC[†]; $x_1 = x_1^H$: symmetry[‡]	
	$x_2 = 0$: ABC[†]; $x_2 = x_2^f$: symmetry[§]	
	$x_3 = 0$: free surface; $x_3 = x_{3end}$: ABC[†]	
Fault Constitutive Parameters		
Initial rake angle, φ_0	0°[∥]	
Magnitude of the initial shear stress, τ_0	73.8 MPa	63.88 MPa
Magnitude of the effective normal stress, σ_n^{eff}	120 MPa	
Static level of friction coefficient, μ_u	0.677 ($\leftrightarrow \tau_u = 81.24$ MPa)	
Kinetic level of friction coefficient, μ_f	0.46 ($\leftrightarrow \tau_f = 55.2$ MPa)	
Dynamic stress drop, $\Delta\tau_d \underset{df}{=} \tau_0 - \tau_f$	18.6 MPa	8.68 MPa
Strength parameter, S	0.4	2
Characteristic slip-weakening distance, d_0	0.4 m[#]	

*Dimensions of the fault guarantee the transition up to supershear speeds in the case of a low-strength fault; extrapolating results from Dunham (2007; his figures 5 and 10) yields $L^f > L_c \equiv \frac{1}{4\alpha(S)}\frac{Gd_0}{\tau_u - \tau_f} = 3.072$ km and $W^f > W_c \cong 0.4L_c = 1.229$ km.

[†]The absorbing boundary conditions are described in detail in Bizzarri and Spudich (2008; their appendix A).

[‡]The symmetry about the strike location of the hypocenter ($x_1 = x_1^H$) is exploited as described in Bizzarri (2009a): (i,j,k) denotes the triplet identifying a node in the $Ox_1x_2x_3$ Cartesian coordinate system (see also Fig. 1). The components of the particle velocity will satisfy the following rules: $V_1(+i,j,k) = V_1(-i,j,k)$; $V_2(+i,j,k) = -V_2(-i,j,k)$; $V_3(+i,j,k) = -V_3(-i,j,k)$, where minus and plus signs in front of the i-index denote a point with x_1 coordinates less than and greater than x_1^H, respectively.

[§]The symmetry about the fault ($x_2 = x_2^f$) is exploited as described in Bizzarri (2009a): the components of the particle velocity will satisfy the following rules: $V_1(i,+j,k) = -V_1(i,-j,k)$; $V_2(i,+j,k) = V_2(i,-j,k)$; $V_3(i,+j,k) = -V_3(i,-j,k)$, where minus and plus signs in front of the j–index denotes a point with x_2 coordinates lower and greater than x_2^f, respectively.

[∥]Initial shear traction is aligned along x_1 and defines a left-lateral strike-slip fault.

[#]With this value, I obtain a sufficiently good resolution of the cohesive zone (see Bizzarri and Cocco, 2005). A larger value would imply that rupture will take several kilometers to get started on its own.

However, as apparent in the synoptic comparison between elliptical shear asperities reported in Figure 5, the dynamic propagation is significantly delayed as the size of the shear asperity is reduced (i.e., as the multiplicative factor of $L_c^{(II)}$ and $L_c^{(III)}$ decreases). Just for an example, at the hypocentral depth the rupture tip arrives at a strike distance from H of roughly 5 km at $t = 1.5$ sec for $r_a = 2.2L_c^{(II)}$ ($= r_c^{(D)}$ for my parameters) and at $t = 2.5$ sec for $r_a = 1.45L_c^{(II)}$. This indicates that, in the latter case, the rupture takes more time to be able to propagate on its own outside I_{nucl}.

By construction, the TW-driven rupture is that which better satisfies criteria (2) and (4) and can be regarded as the desired solution. Among the other possibilities pre-sented previously, the case that better agrees with it is the rupture forced with an elliptical asperity (with a static overshoot $\Delta\tau_{nucl} = 0.5\%\tau_u$ in the initial shear stress) with semi-axes $r_a = r_c^{(D)}$ ($= 2.2L_c^{(II)}$ for my parameters) and $r_b = 2.2L_c^{(III)}$.

Results for Subshear Rupture Propagation

The differences between the nucleation strategies become significant in the case of configuration B, the subshear rupture, for which the maximum allowable rupture speed is $v_{r_{max}} = v_R$. The behavior of the rupture is quite sensitive (definitely more than in the case of the supershear rupture

Table 2

Optimal Parameters for the Nucleation Strategies Considered in This Article

Parameter	Value[*]	
	Configuration A ($S = 0.4$)	Configuration B ($S = 2$)
Initially Nonspontaneous Rupture Propagation		
Initially constant rupture velocity, v_{force}	$0.75 v_R$ ($= 2.4$ km/sec)	
Weakening time, t_0	0.1 sec	
Nucleation patch, I_{nucl}	Circle	Circle
Dimension of the nucleation patch	$r = r_c^{(D)}$	$r = 1.57 r_c^{(D)}$
Introduction of an Initial Shear Stress Asperity		
Static overshoot, $\Delta \tau_{nucl}$	$0.5\% \, \tau_u$ ($= 0.4062$ MPa)	
Nucleation patch, I_{nucl}	Ellipse	Smoothed ellipse
Dimensions of the nucleation patch along x_1 and x_3 axes	$r_a = r_c^{(D)}$ $r_b = r_c^{(D)}(L_c^{(III)}/L_c^{(II)})$	$r_a = r_c^{(D)}$ $r_b = r_c^{(D)}(L_c^{(III)}/L_c^{(II)})$, $l_{taper} = 2.6$ km
Perturbation to the Initial Particle Velocity		
Initial fault slip velocity in H, v_0	$20 \, \mu$m/sec	
Sensitivity parameter for tapering of V_i in the x_2 direction, d_{nucl}	20 m	
Nucleation patch, I_{nucl}	Circle	Circle
Dimensions of the nucleation patch along x_1 and x_3 axes	$l_1 = l_2 = r_c^{(D)}$	$l_1 = l_2 = r_c^{(D)}$

*Numerical values inside parentheses are calculated in the case of the adopted models parameters (listed in Table 1).

presented in previous section) to the parameters of each nucleation procedure (see Table 2), as discussed in depth in the Appendix. In the present section, I compare the best cases for the three nucleation strategies described in the Different Nucleation Strategies section.

First, I have verified that, for all the considered nucleation procedures, a nucleation patch with a dimension along x_1 (radius, major semi-axis, or side) equal to $L_c^{(II)}$ is not large enough to produce a dynamic instability that is able to spontaneously propagate over the whole fault. Because in
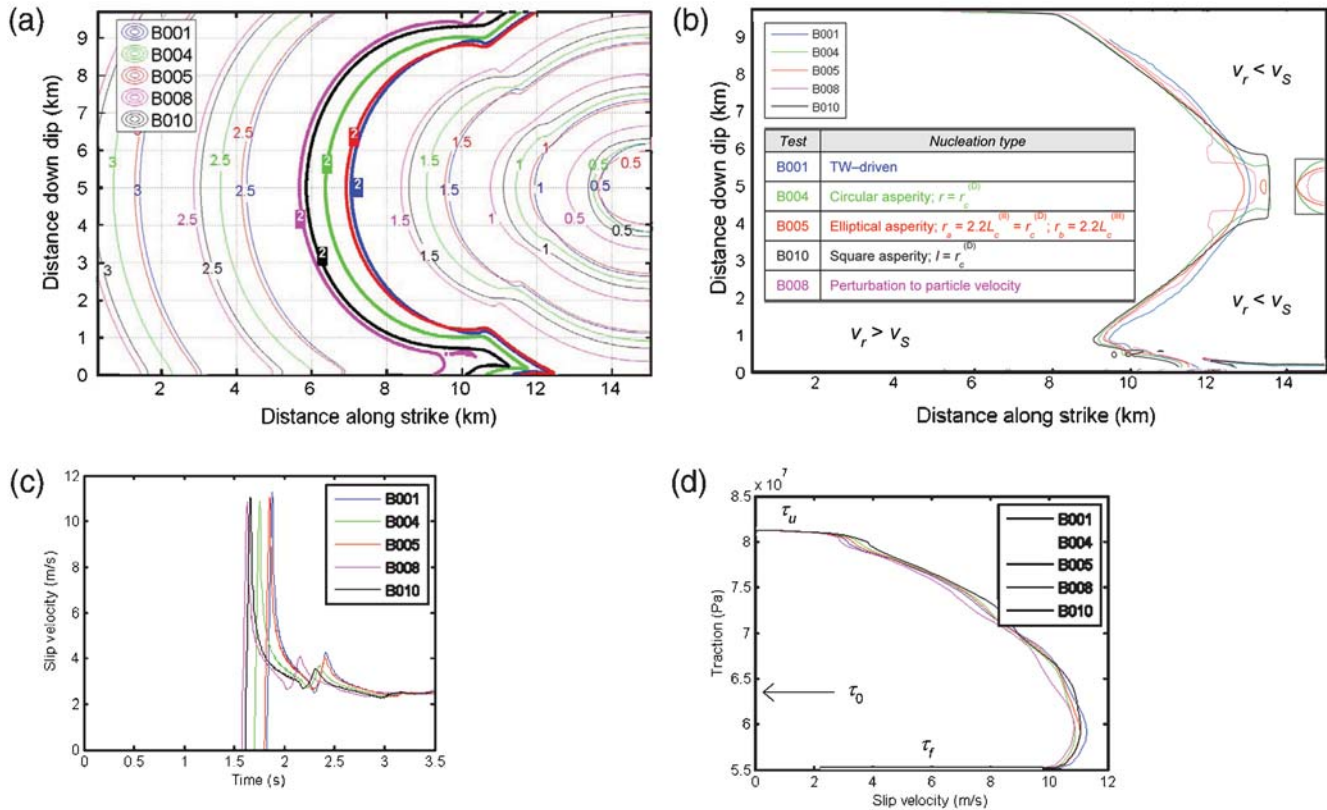

Figure 3. Comparison between solutions for ruptures developing on a low-strength fault ($S = 0.4$) obtained by using different nucleation strategies. (a) Contours of rupture times plotted every 0.5 sec, with rupture times equal to 2 sec reported with thick lines for better clarity. (b) Boundary between supershear and subshear regimes: fault points located on the right of each line experience subshear rupture velocities. (c) Slip velocity time histories. (d) Phase portrait in a fault point located at hypocentral depth and at a distance of 7 km from H.
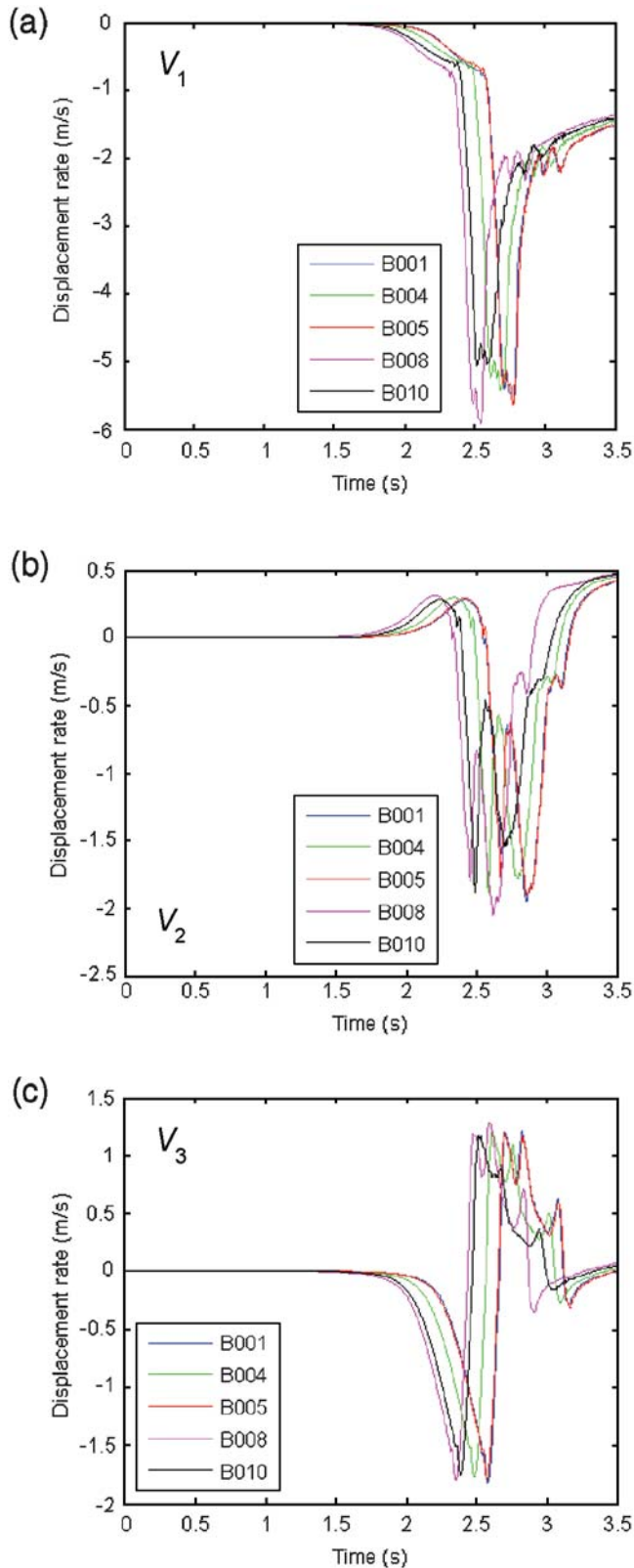
Figure 4. Time histories of the resulting particle velocity for the five models of Figure 3 on a free surface receiver located at a strike distance of 7 km from the epicenter and at a distance of 1 km from the fault trace. (a) Fault-parallel component of $\mathbf{V}$ (namely V_1). (b) Fault-normal component of $\mathbf{V}$ (namely V_2). (c) Vertical component of $\mathbf{V}$ (namely V_3).
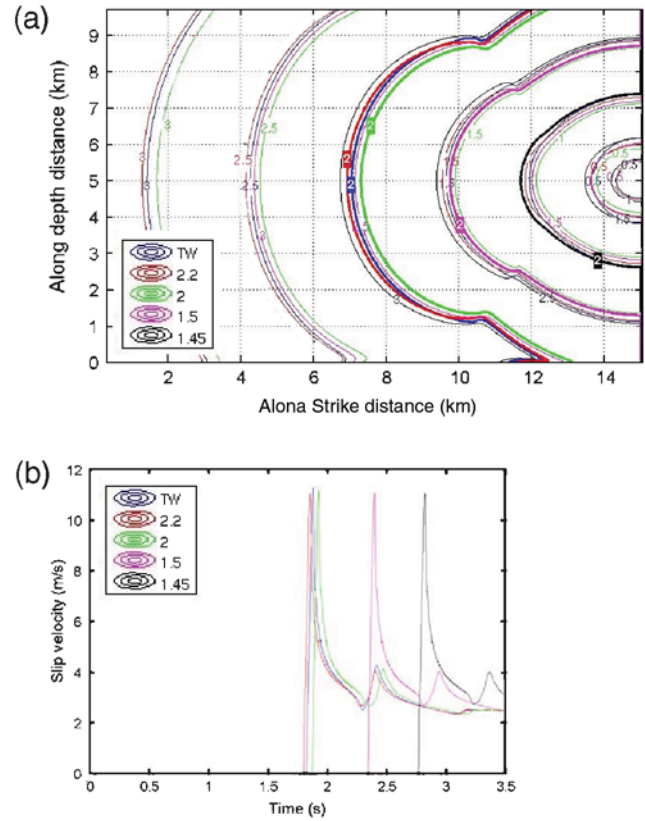
Figure 5. (a) Comparison between rupture times (contour lines plotted every 0.5 sec) for low-strength ruptures nucleating with the imposition of an initial shear asperity of elliptical shape and having different values of the major and minor semi-axes: $r_a = \alpha L_c^{(II)}$ and $r_b = \alpha L_c^{(III)}$. The values of the multiplicative factor of α are indicated in the legends. The case $\alpha = 1.5$ roughly corresponds to having semi-axes equal to critical values of Uenishi and Rice (2004; see equations (4) and (5). (Namely, $r_a = a_c^{(UR)}$ when $\alpha = 1.56$). To emphasize the different locations of the rupture tip in the various numerical experiments, the curves corresponding to 2 sec are displayed with thick lines. (b) Time evolution of the slip velocity in the same fault point of Figures 3c and 3d. The result of the initially TW-driven rupture (blue line) is reported in both panels for comparison.

this case $a_c^{(UR)} < L_c^{(II)}$ (see Table 3), the same is true when I_{nucl} extends $a_c^{(UR)}$ along x_1. Again, this is physically reasonable because $L_c^{(II)}$ and $L_c^{(III)}$ were derived in 2D.

In Figure 6a there is a comparison between rupture times obtained for a TW-driven rupture (I_{nucl} of equation 7 is now a circle with radius $1.57r_c^{(D)}$; blue curve), for two smoothed asperities (circular, green line; elliptical, red line), and for the case of perturbation of particle velocity (magenta line). In the case of smoothed asperities, I assume that τ_{nucl} of equation (9) overcomes (by the overshoot $\Delta\tau_{\mathrm{nucl}}$) τ_u only in an inner portion of I_{nucl}, and it is cosine-tapered to τ_0 at $\partial I_{\mathrm{nucl}}$ over the length $l_{\mathrm{taper}} = 2.6$ km. In the case of the smoothed circular asperity, τ_{nucl} exceeds τ_0 in a circular region of radius $r = r_c^{(D)}$ (see Fig. 6b,c); in the case of the smoothed elliptical asperity, τ_{nucl} exceeds τ_0 in an elliptical region with $r_a = r_c^{(D)}$ ($= 2.2L_c^{(II)}$ for my parameters) and

$r_b = 2.2L_c^{(III)}$. Fig. 6a clearly shows a delay in the rupture times and also a significant difference in the peaks of the resulting fault slip velocity (Fig. 6d). On the contrary, in the case of configuration A, the peaks in fault slip velocity were substantially the same (see Fig. 3c).

The comparison of the free surface velocity histories (Fig. 7) shows that the nucleation obtained by imposing a perturbation in the initial particle velocity (magenta lines) causes the solutions to be more oscillating for early times ($t < 3$ sec for this receiver); such high frequency oscillations are spurious artifacts that are absent in the solutions obtained by using the other nucleation strategies. These oscillations are present also in the distributions of the rupture velocity (see Figs. A3a and A3b in the Appendix) and are in contrast with criterion (2).

Among the different solutions, the TW-driven nucleation over a region of radius $r > r_c^{(D)}$ and with $v_{force} = 0.75v_R$ and $t_0 = 0.1$ s is that which better satisfies criteria in the Quantitative Criteria for the Evaluation of the Nucleation Strategy section and therefore can be regarded as the desired solution. The other solution that better approaches this behavior corresponds to the smoothed elliptical shear stress asperity, with semi-axes $r_a = r_c^{(D)}$, $r_b = r_c^{(D)} \frac{L_c^{(III)}}{L_c^{(II)}}$, and $l_{taper} = 2.6$ km. The specific values of r (in the case of TW-driven rupture) and l_{taper} (when asperity is imposed) can depend on the adopted constitutive parameters; their optimal values might have to be numerically obtained by a trial-and-error approach.

Discussion and Concluding Remarks

The numerical simulation of rupture dynamics is fundamental in the attempt to understand earthquake physics and in strong ground-motion prediction. Coherent modeling of earthquake rupture requires the description of the several space and time scales involved in the rupturing process, such as the nucleation (an initial, aseismic slippage, where inertial effects are negligible), the rapid propagation of the rupture (seismically detectable and associated with the emission of seismic waves and with the stress redistribution in the sur-

roundings of the fault), and the rupture arrest. Space and time steps are numerically controlled by the smallest scale; the nucleation therefore requires very small computational grids as compared to the rest of the process and drastically increases the computation time, even if the nucleation zone is very small compared to the surface which fails. Moreover, the time duration of the nucleation is very much longer than that of cosesimic processes. As indicated previously, my main interest here is not on the physical details of the nucleation process, which can be modeled by considering a tectonically driven fault (see for instance Liu and Lapusta, 2008). Because my focus is on the dynamic rupture propagation, it is computationally convenient to introduce artificial processes that allow the rupture to spontaneously propagate. Nevertheless, the correct modeling of the nucleation is fundamental to properly retrieve the slip and rupture time distribution on the fault plane, as well as to model the energy content of the radiation and its distribution in the frequency domain.

In this article, I have considered 3D dynamic ruptures spontaneously spreading on a planar fault, which obey the linear slip-weakening (SW) law (equation 6) and which are embedded in a homogeneous, elastic medium, free from external tectonic loading. I have considered various nucleation strategies, largely employed in the literature, that are conceptually and algorithmically different: the initially nonspontaneous, time-weakening (TW)–driven rupture propagation (the Initially Nonspontaneous Rupture Propagation section); the introduction of an asperity in the initial shear stress (the Introduction of an Initial Shear Stress Asperity section); and the perturbation to the initial particle velocity (the Perturbation to the Initial Particle Velocity section). I have systematically compared the resulting solutions by considering the agreement with respect to a desired solution, and the latter is the solution that better satisfies all the criteria described in the Quantitative Criteria for the Evaluation of the Nucleation Strategy section. I have also tested the effects of the size and of the shape of the initialization zone, I_{nucl}. In the comparison of the solutions, I have considered the rupture times (t_r), the rupture velocities (v_r), the solutions

Table 3
Values of the Critical Nucleation Lengths for the Model Parameters listed in Table 1

| Parameter		Equation in Article Text	Value	
			Configuration A ($S = 0.4$)	Configuration B ($S = 2$)
$L_c^{(II)}$	Critical nucleation in the inplane (x_1) direction, following Andrews (1976b)	(1)	409 m	1880 m
$L_c^{(III)}$	Critical nucleation in the antiplane (x_3) direction, following Andrews (1976a)	(2)	307 m	1410 m
$r_c^{(D)}$	Critical nucleation radius, following Day (1982)	(3)	884 m	4058 m
$a_c^{(UR)}$	Critical nucleation major semi-axis, following Uenishi and Rice (2004)	(4)	639 m	639 m
$b_c^{(UR)}$	Critical nucleation minor semi-axis, following Uenishi and Rice (2004)	(5)	480 m	480 m
$\min\left\{L_c^{(II)}, r_c^{(D)}, a_c^{(UR)}\right\}$			$L_c^{(II)}$	$a_c^{(UR)}$
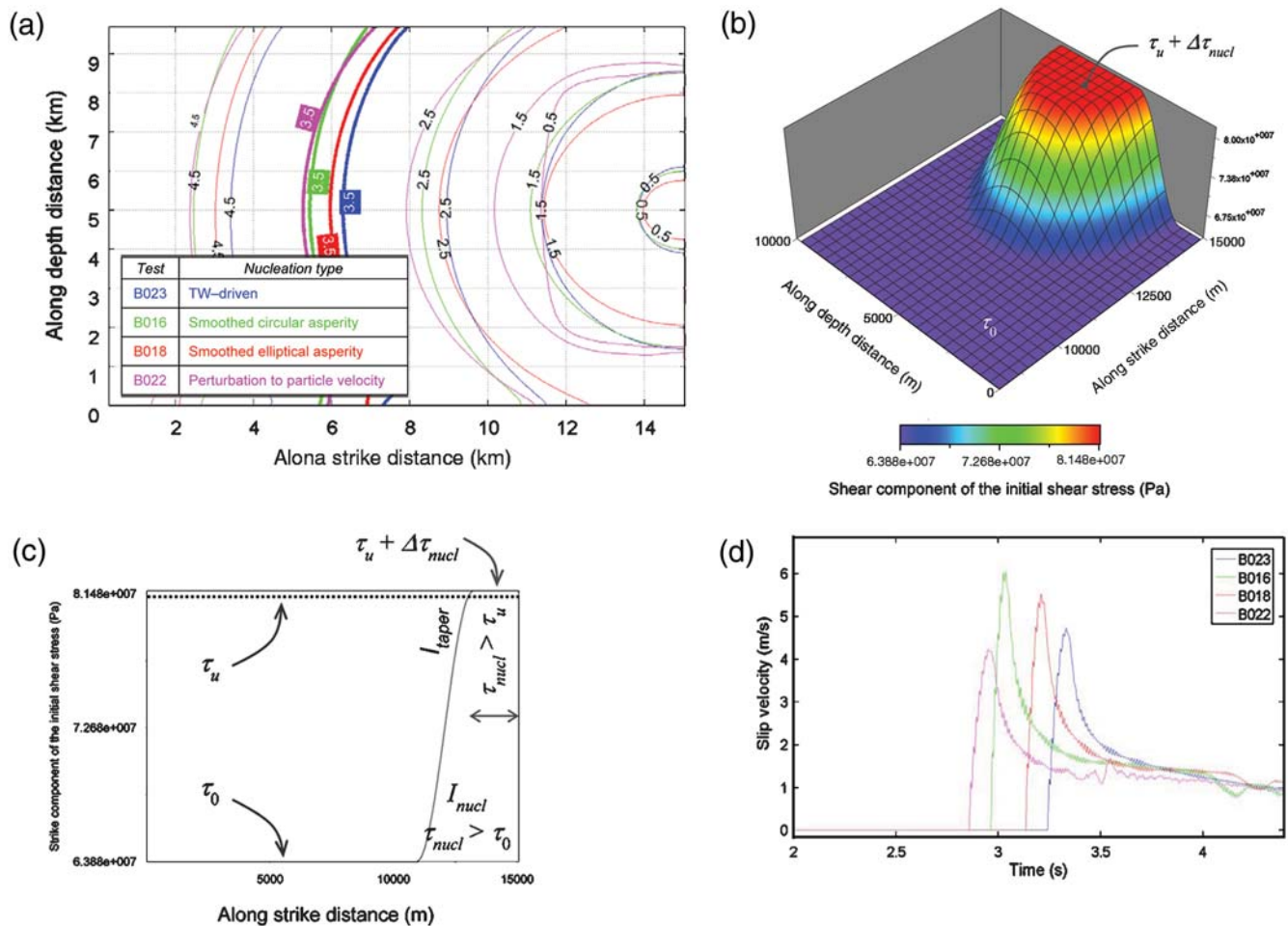
Figure 6. (a) Comparison between rupture times (lines plotted every second) obtained in the case of ruptures developing on a high-strength fault ($S = 2$). Blue line refers to an initially TW-driven event (I_{nucl} of equation 7 is a circle with $r = 1.57 r_c^{(D)}$, $t_0 = 0.1$ sec, and $v_{force} = 0.75 v_R$ [$= 2.4$ km/sec for my parameters]). Green line refers to a solution where a smoothed circular asperity is applied, as reported in panels (b) and (c): $\tau_{nucl} > \tau_0$ in a circular region with $r = r_c^{(D)}$ and $\tau_{nucl} = \tau_u + \Delta\tau_{nucl}$ only in an inner portion of I_{nucl}, and it is cosine-tapered to τ_0 at ∂I_{nucl} over the length $l_{taper} = 2.6$ km. Red line refers to the case of a smoothed elliptical asperity (analogous to previous case but now with major semi-axis $r_a = r_c^{(D)}$ and minor semi-axis $r_b = r_c^{(D)} \frac{L_c^{(III)}}{L_c^{(II)}}$). (d) Comparison between fault slip velocity histories at the a fault point located at hypocentral depth and at a distance of 8 km from H.

on the fault, and the synthetic motions on the free surface of the resulting dynamic ruptures.

One interesting conclusion is that, in the case of super-shear ruptures, the previously mentioned nucleation strategies produce results not dramatically dissimilar one from the others (see the Results from Numerical Experiments: Super-shear Rupture Propagation section). Basically, different strategies lightly change the time occurrence of the transition to supershear rupture speeds (see Fig. 3b), in agreement with the results of Festa and Villotte (2006) and Liu and Lapusta (2008). Interestingly, my results indicate that supershear ruptures tend to forget their origins more than subshear ruptures do. In fact, in the case of ruptures that develop with a speed equal to a fraction of the shear wave velocity, which seem to represent the majority of real-world earthquake events (e.g., Heaton, 1990), the modeler has to carefully tune the param-

eters of each individual nucleation strategy (see the Results for Subshear Rupture Propagation section and the Appendix).

My results also demonstrate that, among the different critical nucleation lengths introduced in the literature (see the Critical Lengths for Nucleation section), the key parameter to be used to quantify the extension of I_{nucl} is $r_c^{(D)}$ (equation 3). For I_{nucl} having a length along the inplane direction less than $r_c^{(D)}$, the rupture does not spontaneously propagate outside the nucleation patch or quickly dies a few fault nodes outside I_{nucl} (contradicting criterion 4). I know that there is a conceptual problem in applying the critical length theoretically derived for 2D geometries to 3D problems. I have performed these tests to numerically verify this because some authors (e.g., Galis *et al.*, 2010) claim that even in 3D the size of I_{nucl} has to be quantified trough multiples of $L_c^{(II)}$ and $L_c^{(III)}$ for both subshear and supershear ruptures.
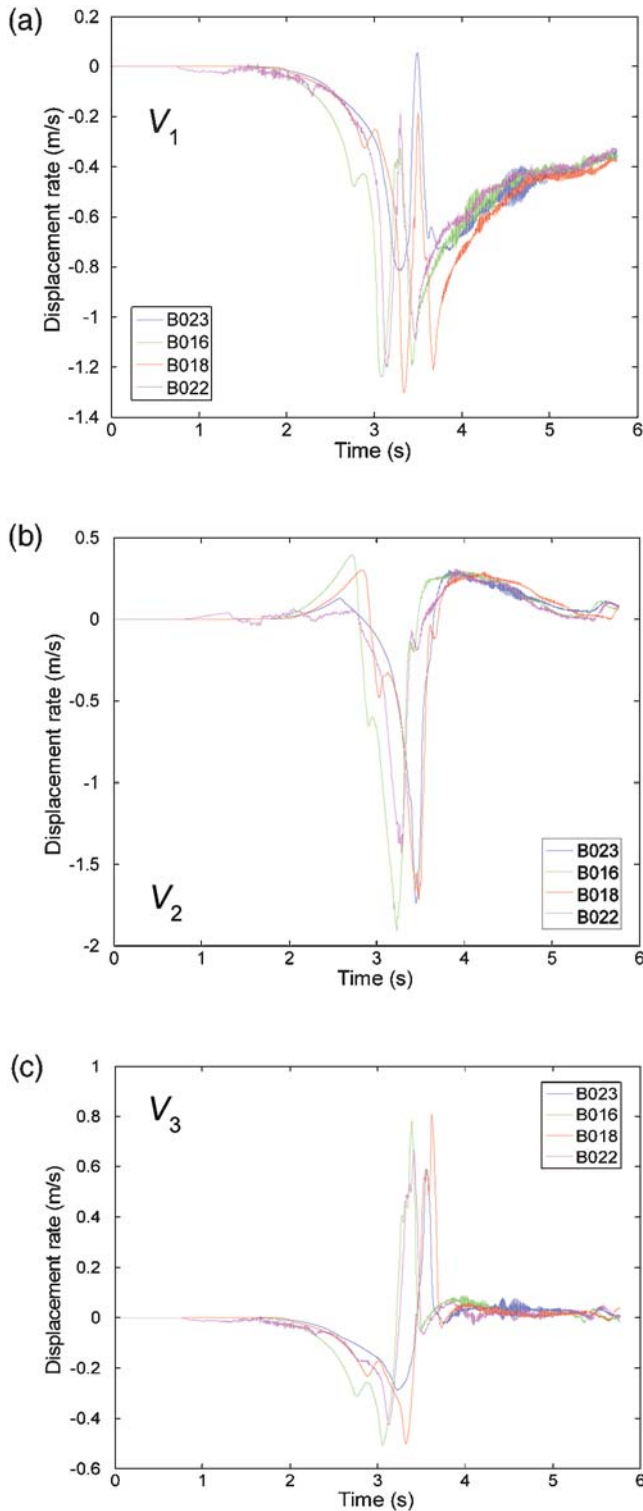
Figure 7. The same as in Figure 4 but for configuration B.

The numerical simulations presented in this article confirm that the TW-driven nucleation strategy, with $v_{\text{force}} = 0.75 v_R$ and $t_0 = 0.1$ sec, produces the desired solution when the size of I_{nucl} along the inplane direction (namely where the condition of equation 7 is evaluated) is $r_c^{(D)}$ for supershear ruptures and greater than $r_c^{(D)}$ in the case of subshear ones.

Moreover, I found that the desired solution is approached when a smoothed elliptical asperity in the initial shear stress is adopted. While the smoothing of the asperity (i.e., the portion of I_{nucl} where τ_{nucl} is gradually tapered from $\tau_u + \Delta\tau_{\text{nucl}}$ to τ_0) is of secondary importance in the case of supershear ruptures, I have shown that the smoothing distance l_{taper} in the case of subshear ruptures is important (see Appendix). I found that the optimal parameters are a static overshoot $\Delta\tau_{\text{nucl}}$ equal to 0.5% of τ_u (in agreement with Liu and Lapusta, 2008, who use 1% of τ_u) and major and minor semi–axes of I_{nucl} given by $r_a = r_c^{(D)}$ and $r_b = r_c^{(D)} \frac{L_c^{(\text{III})}}{L_c^{(\text{II})}}$, respectively. Numerical results indicate that the optimal value of l_{taper} is 2.6 km, but its specific value might change by varying the models parameters; therefore, it has to be found by a trial-and-error procedure. I want to emphasize that, within I_{nucl}, these two nucleation strategies (TW-driven and asperity) have different Kostrov energies (Kostrov and Das, 1988): in the first case, when the rupture propagates at the fixed velocity v_{force}, the Kostrov term is $(\tau_0 - \tau_f)u$, while in the second case, because the initial traction is raised up to τ_u, it is $(\tau_u - \tau_f)u$.

The third type of nucleation strategy is conceptually interesting because it consists of the introduction of a perturbation of the initial reference state of the fault system (the static equilibrium) within a volume surrounding the fault. This is particularly appealing because I have various evidence of the complexity of a fault structure and am aware that a plane is only a mathematical approximation of the volume where nonelastic processes take place (see Bizzarri, 2009b and references therein for a comprehensive discussion). In spite of this, the adoption of this nucleation strategy produces results close to the "desired" solution for supershear ruptures but not for subshear ones. In the latter configuration, the results are in conflict with criterion (2) because they are affected by large, high frequency, spurious oscillations (see Fig. 7) that can not be removed even with a careful exploration of the parameter space.

Different nucleation procedures potentially have different stress drops within the initialization zone. A quantitative estimate of the significant differences caused by the various strategies and, for the same numerical procedure, by the adoption of different values of the nucleation parameters, is represented by the temporal evolution of the (dynamic) seismic moment, $M(t)$, which accounts for the cracked area and for the developed cumulative fault slip during the considered time window. It is expressed as

$$M(t) = \sqrt{M_{21}(t)^2 + M_{23}(t)^2},$$

being

$$M_{2i}(t) \underset{\text{df}}{=} \iint_{\Sigma} G u_i(x_1, x_3, t) dx_1 dx_3,$$

where $i = 1$ and 3, Σ is the fault, and u_1 and u_3 are two components of fault slip (see Bizzarri and Belardinelli,
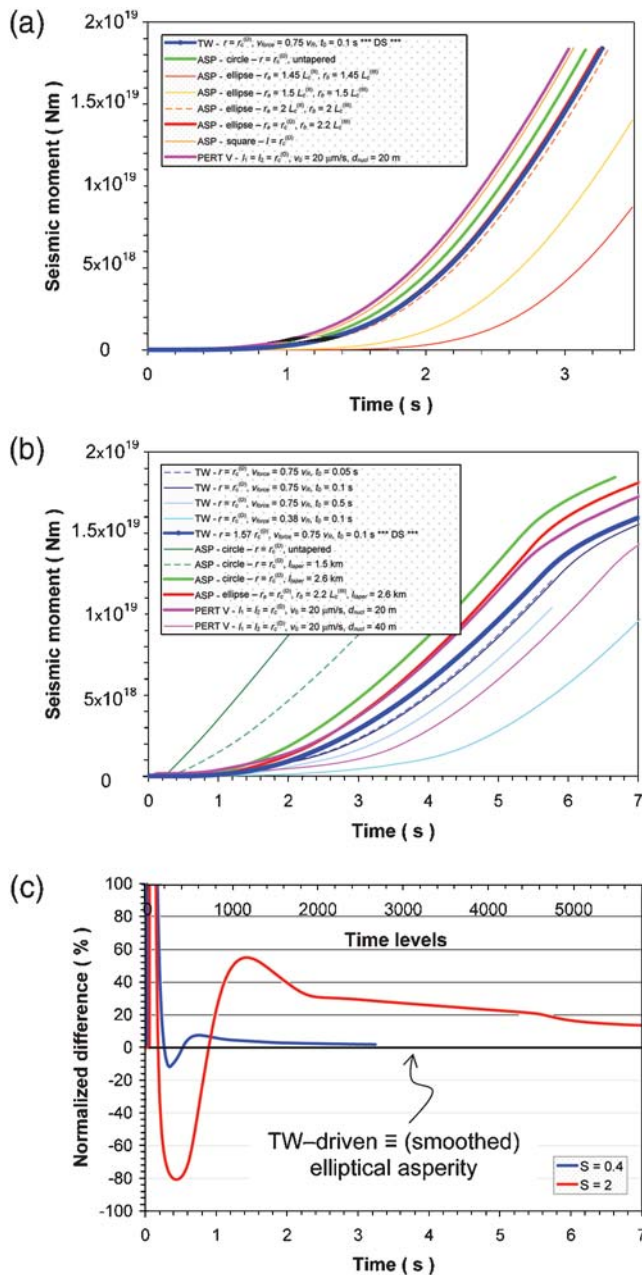
Figure 8. (a) Temporal evolution of the (dynamic) seismic moment, $M(t)$, for different nucleation strategies and for various values of the nucleation parameters in the case of configuration A. (b) The same as panel (a), but in the case of configuration B. Blue lines refer to TW–driven ruptures, green curves to nucleation with circular asperity, red curve to nucleation with elliptical asperity and magenta ones to nucleation with perturbation to **V**. The optimal cases for each type of nucleation strategy are plotted with thick lines. The "desired" solution (marked as "DS" in the legend) is plotted with the thickest blue line. (c) Temporal evolution of the percent differences of seismic moments obtained by adopting the TW–driven nucleation and the (smoothed) elliptical asperity (namely, in the ordinate axis, I plot: $100 \frac{M^{(ASP)}(t) - M^{(TW)}(t)}{M^{(TW)}(t)}$). In the cases of shear asperity, all the fault point where $\tau_{\mathrm{nucl}} \geq \tau_u$ start to move immediately at $t = 0$; this causes the big differences in the first time levels. On the top of the horizontal axis I have also indicated the time levels corresponding to times reported on the bottom horizontal axis.

2008 for further details). A synoptic comparison between $M(t)$ pertaining to the whole ensemble of the numerical experiments presented in this article is reported in Fig. 8. In panels (a) and (b) of that figure the thick lines refer to the optimal cases for each nucleation strategy, that is, the configurations that, for that nucleation strategy, better approaches the desired solution (marked as DS in the legend and plotted with the thickest blue line). In the case of configuration B (subshear ruptures), the tuning of the nucleation parameters reduces the large differences between the results obtained with the various nucleation strategies and the desired solution. While in the case of configuration A (supershear ruptures), the maximum of the absolute value of the difference between the seismic moment obtained with TW-driven nucleation and elliptical shear asperity is of the order of 10%; in the case of configuration B, it increase up to 80% (Fig. 8c). After about 1 sec, the solutions are very similar in the supershear case, while they differ by nearly 30% after about 2 sec in the subshear case.

Finally, I want to highlight that the results of a dynamic model of a synthetic earthquake can be potentially affected and biased from the adoption of a nucleation strategy for linear slip-weakening governing law. This can be due, for instance, to an improper size or shape of the initialization patch, to an excessively high static overshoot, or to an incorrect forcing rupture velocity. This is true especially in the case of high-strength faults; in some configurations, I have found that a huge initial shear stress asperity can lead to the crack front bifurcation at depth and to the transition to supershear rupture speeds, contradicting criterion (3).

As an overall conclusion, I point out that the modeler has to carefully check the obtained numerical solution, compare it against other results and painstakingly tune the nucleation parameters. In this article, I have presented some practical recipes with the aim to serve as guidance in performing these efforts.

Data and Resources

All data sources are taken from published works listed in the References. OpenMP may be accessed at http://openmp.org/wp/.

Acknowledgments

References

Andrews, D. J. (1976a). Rupture propagation with finite stress in antiplane strain, *J. Geophys. Res.* **81,** no. 20, 3575–3582.

Andrews, D. J. (1976b). Rupture velocity of plane strain shear cracks, *J. Geophys. Res.* **81,** no. 32, 5679–5687.

Andrews, D. J. (1985). Dynamic plane-strain shear rupture with a slip-weakening friction law calculated by a boundary integral method, *Bull. Seismol. Soc. Am.* **75,** no. 1, 1–21.

Badea, L., I. R. Ionescu, and S. Wolf (2004). Domain decomposition method for dynamic faulting under slip-dependent friction, *J. Comput. Phys.* **201,** 487–510.

Barenblatt, G. I. (1962). The mathematical theory of equilibrium cracks in brittle fracture, *Adv. Appl. Mech.* **7,** 55–129.

Benioff, H. (1951). Earthquakes and rock creep, Part I: Creep characteristics of rocks and the origin of aftershocks, *Bull. Seismol. Soc. Am.* **41,** 31–62.

Bilby, B. A., A. H. Cottrell, and K. H. Swindon (1963). The spread of plastic yield from a notch, *Proc. R. Soc. London*, Ser. A272, 304–314.

Bizzarri, A. (2009a). Can flash heating of asperity contacts prevent melting?, *Geophys. Res. Lett.* **36,** L11304, doi 10.1029/2009GL037335.

Bizzarri, A. (2009b). What does control earthquake ruptures and dynamic faulting? A review of different competing mechanisms, *Pure Appl. Geophys.* **166,** nos. 5–7, doi 10.1007/s00024-009-0494-1, 741–776.

Bizzarri, A. (2010). Toward the formulation of a realistic fault governing law in dynamic models of earthquake ruptures, in *Dynamic Modelling*, Alisson V. Brito (Editor), IN-TECH, Vienna (Austria), ISBN 978-953-7619-68-8, 167–188.

Bizzarri, A., and M. E. Belardinelli (2008). Modelling instantaneous dynamic triggering in a 3-D fault system: Application to the 2000 June South Iceland seismic sequence, *Geophys. J. Int.* **173,** 906–921, doi 10.1111/j.1365-246X.2008.03765.x.

Bizzarri, A., and M. Cocco (2005). 3D dynamic simulations of spontaneous rupture propagation governed by different constitutive laws with rake rotation allowed, *Ann. Geophys.* **48,** no. 2, 279–299.

Bizzarri, A., and M. Cocco (2006). Comment on "Earthquake cycles and physical modeling of the process leading up to a large earthquake" by M. Ohnaka, *Earth Planets Space* **58,** 1525–1528.

Bizzarri, A., and P. Spudich (2008). Effects of supershear rupture speed on the high-frequency content of *S* waves investigated using spontaneous dynamic rupture models and isochrone theory, *J. Geophys. Res.* **113,** no. B05304, doi 10.1029/2007JB005146.

Bizzarri, A., M. Cocco, D. J. Andrews, and E. Boschi (2001). Solving the dynamic rupture problem with different numerical approaches and constitutive laws, *Geophys. J. Int.* **144,** 656–678.

Bizzarri, A., E. M. Dunham, and P. Spudich (2010). Coherence of Mach fronts during heterogeneous supershear earthquake rupture propagation: Simulations and comparison with observations, *J. Geophys. Res.* (in press).

Burridge, R., G. Conn, and L. B. Freund (1979). The stability of a rapid mode II shear crack with finite cohesive traction, *J. Geophys. Res.* **85,** no. B5, 2210–2222.

Cocco, M., and A. Bizzarri (2002). On the slip-weakening behavior of rate- and state dependent constitutive laws, *Geophys. Res. Lett.* **29,** no. 11, doi 10.1029/2001GL013999.

Day, S. M. (1982). Three-dimensional finite difference simulation of fault dynamics: Rectangular faults with fixed rupture velocity, *Bull. Seismol. Soc. Am.* **72,** 705–727.

Dieterich, J. H. (1979). Modelling of rock friction: 1. Experimental results and constitutive equations, *J. Geophys. Res.* **84,** 2161–2168.

Dugdale, D. S. (1960). Yielding of steel sheets containing slits, *J. Mech. Phys. Solids* **8,** 100–104.

Dunham, E. M. (2007). Conditions governing the occurrence of supershear ruptures under slip-weakening friction, *J. Geophys. Res.* **112,** no. B07302, doi 10.1029/2006JB004717.

Dunham, E. M., and H. S. Bhat (2008). Attenuation of radiated ground motion and stresses from three-dimensional supershear ruptures, *J. Geophys. Res.* **113,** no. B08319, doi 10.1029/2007JB005182.

Ellsworth, W. L., and G. C. Beroza (1995). Seismic evidence for an earthquake nucleation phase, *Science* **268,** 851–855.

Festa, G., and J.-P. Vilotte (2006). Influence of the rupture initiation on the intersonic transition: Crack-like versus pulse-like modes, *Geophys. Res. Lett.* **33,** L15320.

Galis, M., P. Moczo, J. Kristek, and M. Kristekova (2010). An adaptive smoothing algorithm in the TSN modeling of rupture propagation with the linear slip-weakening friction law, *Geophys. J. Int.* **180,** 418–432, doi 10.1111/j.1365-246X.2009.04427.x.

Harris, R. A., R. J. Archuleta, B. Aagaard, J. P. Ampuero, D. J. Andrews, L. Dalguer, S. M. Day, E. M. Dunham, G. Ely, Y. Kase, N. Lapusta, Y. Liu, S. Ma, D. Oglesby, K. B. Olsen, and A. Pitarka (2004). The source physics of large earthquakes—Validating spontaneous rupture methods, *Eos Trans. AGU* **85,** no. 47, Fall Meet. Suppl., Abstract S12A-05.

Harris, R. A., M. Barall, R. J. Archuleta, E. M. Dunham, B. Aagaard, J. P. Ampuero, H. Bhat, V. M. Cruz-Atienza, L. Dalguer, P. Dawson, S. M. Day, B. Duan, G. Ely, Y. Kaneko, Y. Kase, N. Lapusta, Y. Liu, S. Ma, D. Oglesby, K. B. Olsen, A. Pitarka, S. Song, and E. Templeton (2009). The SCEC/USGS dynamic earthquake rupture code verification exercise, *Seism. Res. Lett.* **80,** no. 1, doi 10.1785/gssrl.80.1.119, 119–126.

Heaton, T. H. (1990). Evidence for and implications of self-healing pulses of slip in earthquake rupture, *Phys. Earth Planet. In.* **64,** 1–20.

Ida, Y. (1972). Cohesive force across the tip of a longitudinal-shear crack and Griffith's specific surface energy, *J. Geophys. Res.* **77,** no. 20, 3796–3805.

Iio, Y. (1995). Observations of slow initial phase generated by microearthquakes: Implications for earthquake nucleation and propagation, *J. Geophys. Res.* **100,** no. B8, 15,333–15,349.

Ionescu, I. R., and M. Campillo (1999). Influence of the shape of the friction law and fault finiteness on the duration of initiation, *J. Geophys. Res.* **104,** no. B2, 3013–3024.

Kanamori, H. (1981). The nature of seismicity patterns before large earthquakes, in *Earthquake Prediction—An International Review*, Maurice Ewing Series 4, D. W. Simsone and P. G. Richards (Editors), American Geophysical Union, Washington, D.C., 1–19.

Kilb, D., and J. Gomberg (1999). The initial subevent of the 1994 Northridge, California, earthquake: Is earthquake size predictable?, *J. Seismol.* **3,** 409–420.

Kostrov, B. V., and S. Das (1988). *Principles of Earthquake Source Mechanics*, Cambridge University Press, New York, 286 pp.

Lapusta, N., and J. R. Rice (2003). Nucleation and early seismic propagation of small and large events in a crustal earthquake model, *J. Geophys. Res.* **108,** no. B4, 2205, doi 10.1029/2001JB000793.

Lapusta, N., J. R. Rice, Y. Ben-Zion, and G. Zheng (2000). Elastodynamic analysis for slow tectonic loading with spontaneous rupture episodes on faults with rate- and state-dependent friction, *J. Geophys. Res.* **105,** 23,765–23,789.

Liu, Y., and N. Lapusta (2008). Transition of mode II cracks from sub-Rayleigh to intersonic speeds in the presence of favorable heterogeneities, *J. Mech. Phys. Solid.* **56,** 25–50.

Matsu'ura, M., H. Kataoka, and B. Shibazaki (1992). Slip-dependent friction law and nucleation processes in earthquake rupture, *Tectonophysics* **211,** 135–148.

Reid, H. F. (1910). The mechanics of the earthquake, *The California Earthquake of April 18, 1906, Report of the State Earthquake Investigation Commission*, Vol. II, Lawson, A. C. (Chairman), Carnegie Institute of Washington Publication 87, 192 pp. (reprinted 1969).

Rice, J. R., and M. Cocco (2007). Seismic fault rheology and earthquake dynamics, in *Tectonic Faults: Agents of Change on a Dynamic Earth*, M. R. Handy, G. Hirth, and N. Hovius (Editors), The MIT Press, Cambridge, Massachusetts, 99–137.

Rivera, L., and H. Kanamori (2002). Spatial heterogeneity of tectonic stress and friction in the crust, *Geophys. Res. Lett.* **29,** no. 6, 1088, doi 10.1029/2001GL013803.

Shi, Z., and Y. Ben-Zion (2006). Dynamic rupture on a bimaterial interface governed by slip-weakening friction, *Geophys. J. Int.* **165,** 469–484, doi 10.1111/j.1365-246X.2006.02853.x.

Uenishi, K., and J. R. Rice (2003). Universal nucleation length for slip-weakening rupture instability under nonuniform fault loading, *J. Geophys. Res.* **108,** no. B1, 2042, doi 10.1029/2001JB001681.

Uenishi, K., and J. R. Rice (2004). Three-dimensional rupture instability of a slip-weakening fault under heterogeneous loading, *Eos Trans. AGU* **85,** no. 46, Fall Meet. Suppl., Abstract S13E-04.

Xia, K., A. J. Rosakis, and H. Kanamori (2004). Laboratory earthquakes: The sub-Rayleigh-to-supershear rupture transition, *Science* **303,** 1859–1861.

Appendix

Sensitivity to the Nucleation Parameters

While the differences between ruptures forced to develop using dissimilar nucleation strategies are relatively small in the case of supershear ruptures (see the Results from Numerical Experiments: Supershear Rupture Propagation section), they become more significant in the case of subshear ruptures (see the Results for Subshear Rupture Propagation section). Moreover, the nucleation parameters (listed in Table 2) have important effects on the further dynamic rupture propagation; and, therefore, a thorough tuning of them is required in order to cause a dynamic propagation consistent with all the criteria listed in the Quantitative Criteria for the Evaluation of the Nucleation Strategy section, as discussed in the remainder of this appendix.

The Case of TW-Driven Ruptures

In Figure A1, I compare the solutions obtained by varying the parameters of the TW-driven nucleation. The behavior of the dynamic rupture at a radial distance greater than $1.5r_c^{(D)}$ from H is practically identical in all cases. The most important differences appear at lower hypocentral distances, where the rupture velocity is forced to equal v_{force}. In the cases plotted in Figures A1a to A1d, v_r has large fluctuations near ∂I_{nucl}, which are in contrast with criterion (2) (see the Quantitative Criteria for the Evaluation of the Nucleation Strategy section) and are very difficult to justify physically. When the rupture becomes spontaneous, v_r increases; soon it decreases a lot (blue annular region in Figs. A1a to A1d); and it finally increases again up to its limiting velocity. This indicates that even if the SW law takes over, the solution is still affected by the imposed nucleation. This behavior becomes more evident as t_0 increases (compare Figs. A1a and A1c); from the rupture times reported in Figure A1f, for $t_0 > 0.1$ sec the rupture is affected by a significant delay. The resulting v_r for the desired solution, which better satisfies all criteria in the Quantitative Criteria for the Evaluation of the Nucleation Strategy section, is reported in Figure A1d (corresponding to the blue curve in Figs. 6a, 6d, and 7), in which the radius of I_{nucl} where the condition of equation (6) is evaluated is greater that $r_c^{(D)}$. The specific value of $r = 1.57r_c^{(D)}$ might depend on the adopted governing parameters, and, therefore, it might have to be found numerically by a trial-and-error procedure.

The Case of Initial Stress Asperity

Figure A2 summarizes the comparison between different types of asperities introduced in the initial shear stress field. I first emphasize that, by forcing the rupture by assuming a circular asperity with radius $r = r_c^{(D)}$, the rupture hits the free surface with so much energy as to cause the birth of a sustained supershear pulse, which is in contrast with criterion (3). Moreover, in all cases presented in the previous section, the supershear patch was noticeably smaller, and the supershear pulse died very soon (see Figs. A1 and A3), while in the present case it continues to propagate up to the boundary of the computational domain. These results clearly indicate that, in the case of configuration B, the initial shear stress asperity as defined in equation (9) has to be modified in order to obtain the desired solution. I therefore consider a smoothed asperity as described in the Results for Subshear Rupture Propagation section (see also Fig. 6b,c); I set I_{nucl} with $r = r_c^{(D)}$ and progressively increase l_{taper}. As a consequence of this variation, I also decrease the size of the inner region (having radius $r_c^{(D)} - l_{\text{taper}}$), where $\tau_{\text{nucl}} \geq \tau_u$. Results for two cases are reported in Figures A2b and A2c. By progressively increasing l_{taper}, the supershear patch is reduced. The result that better agrees with the desired solution (that reported in Fig. A1d) corresponds to the smoothed elliptical asperity (Fig. A3d), having $r_a = r_c^{(D)}$, $r_b = r_c^{(D)} \frac{L_c^{(\text{III})}}{L_c^{(\text{II})}}$, and $l_{\text{taper}} = 2.6$ km; a further increase of l_{taper} will cause the rupture to die and to not propagate dynamically outside the initialization zone (and this is barely in contrast with criterion 4). A similar result is obtained with a smoothed circular asperity (Fig. A2c). From the comparison of the rupture times (Fig. A2e), the best agreement is between the configurations of panels (c) and (d), as expected.

Finally, I note a small, semicircular patch at the hypocentral depth that is slightly supershear. This small numerical artifact (which tends to be against criterion 2) becomes larger and more pronounced as the static overshoot $\Delta\tau_{\text{nucl}}$ increases.

The Case of the Perturbation to the Initial Particle Velocity

My numerical simulations indicate that the prominent parameter in this nucleation procedure is d_{nucl}, which controls the extension of the volume in the direction perpendicular to the fault, where $\mathbf{V}$ is perturbed at $t = 0$. If this region is too wide ($d_{\text{nucl}} > 50$ m), the rupture is not able to dynamically propagate outside I_{nucl}, even for large values of v_0; this contradicts criterion 4. In Figure A3 compares the resulting normalized rupture velocities for two of the numerical simulations performed. The rupture decelerates
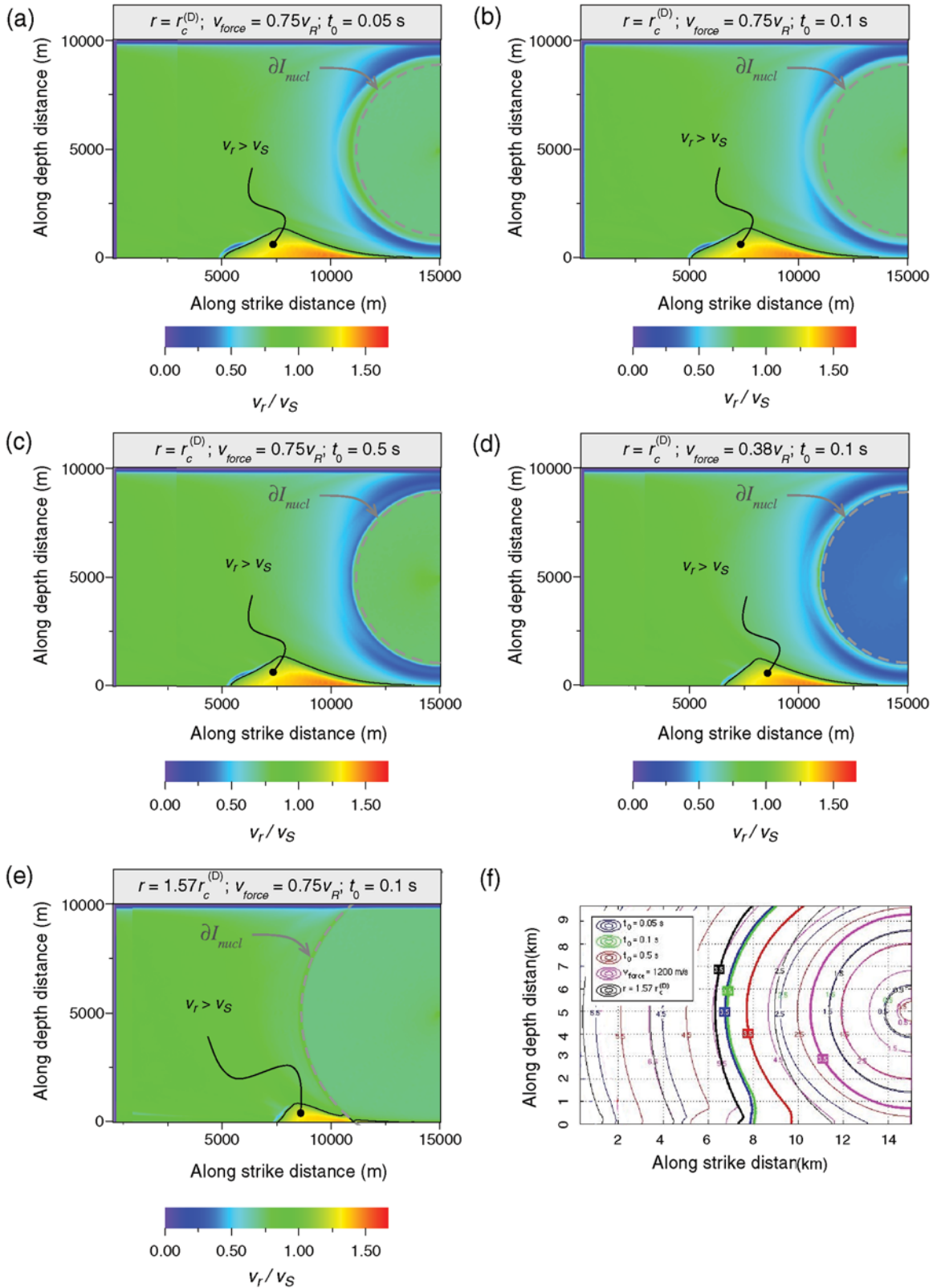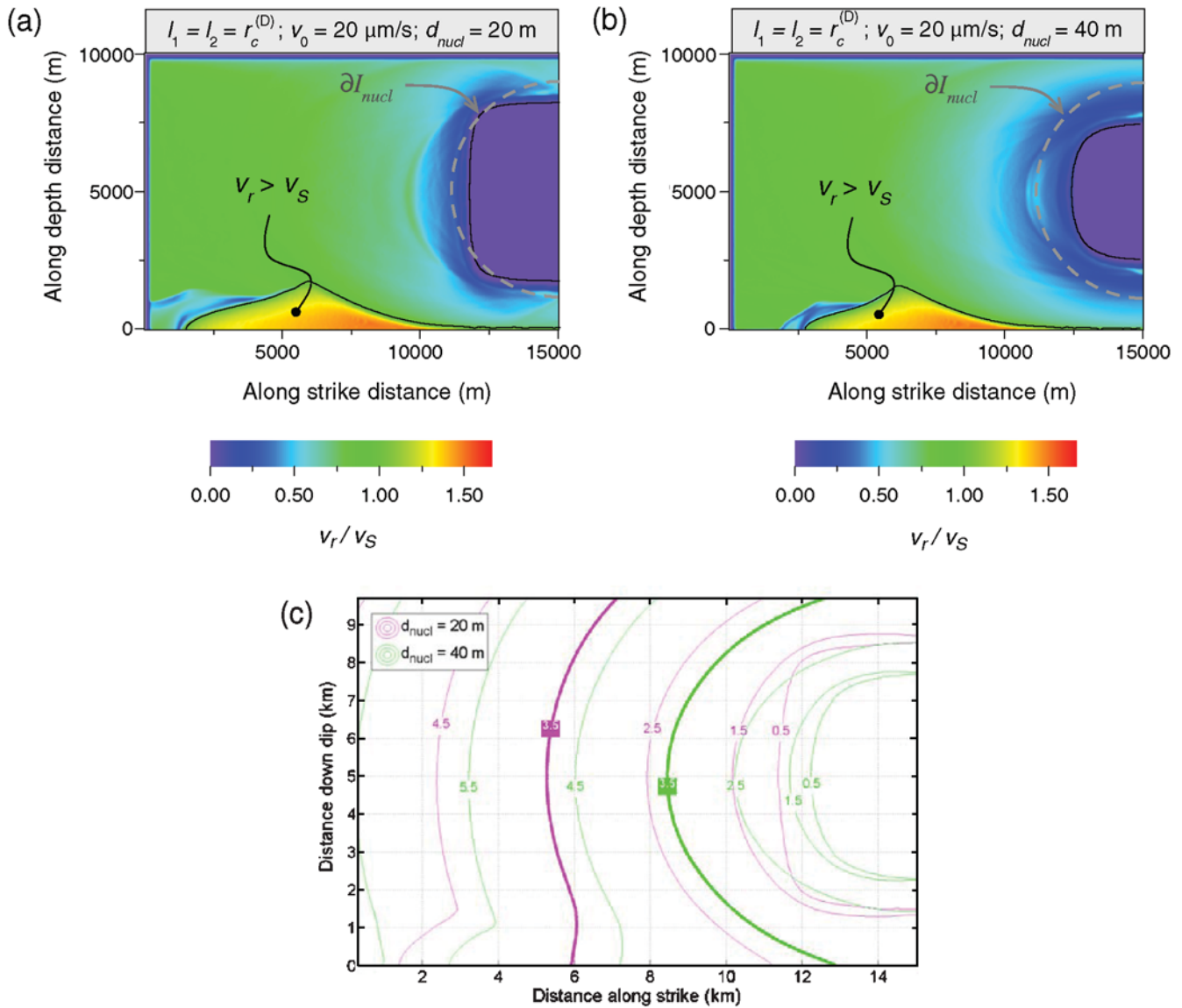
Figure A1. Effects of the nucleation parameters in the case of TW-driven rupture in case of high strength ruptures. Normalized rupture velocity distributions (namely, v_r/v_S) are shown in panel (a) for t_0 of equation (8) equal to 0.05 sec; (b) for $t_0 = 0.1$ sec; (c) for $t_0 = 0.5$ sec; and (d) for $t_0 = 0.1$ sec and $v_{force} = 1.2$ km/sec. In all these numerical experiments, $r = r_c^{(D)}$. (e) Refers to a case with $t_0 = 0.1$ sec and $r = 1.57 r_c^{(D)}$. (f) Resulting rupture times for all tests reported in previous panels, where the curves corresponding to 3.5 sec are displayed with thick lines for a better comparison. In panels (a) to (e), fault patches where v_r is locally supershear are indicated, as well as the extension of I_{nucl}.
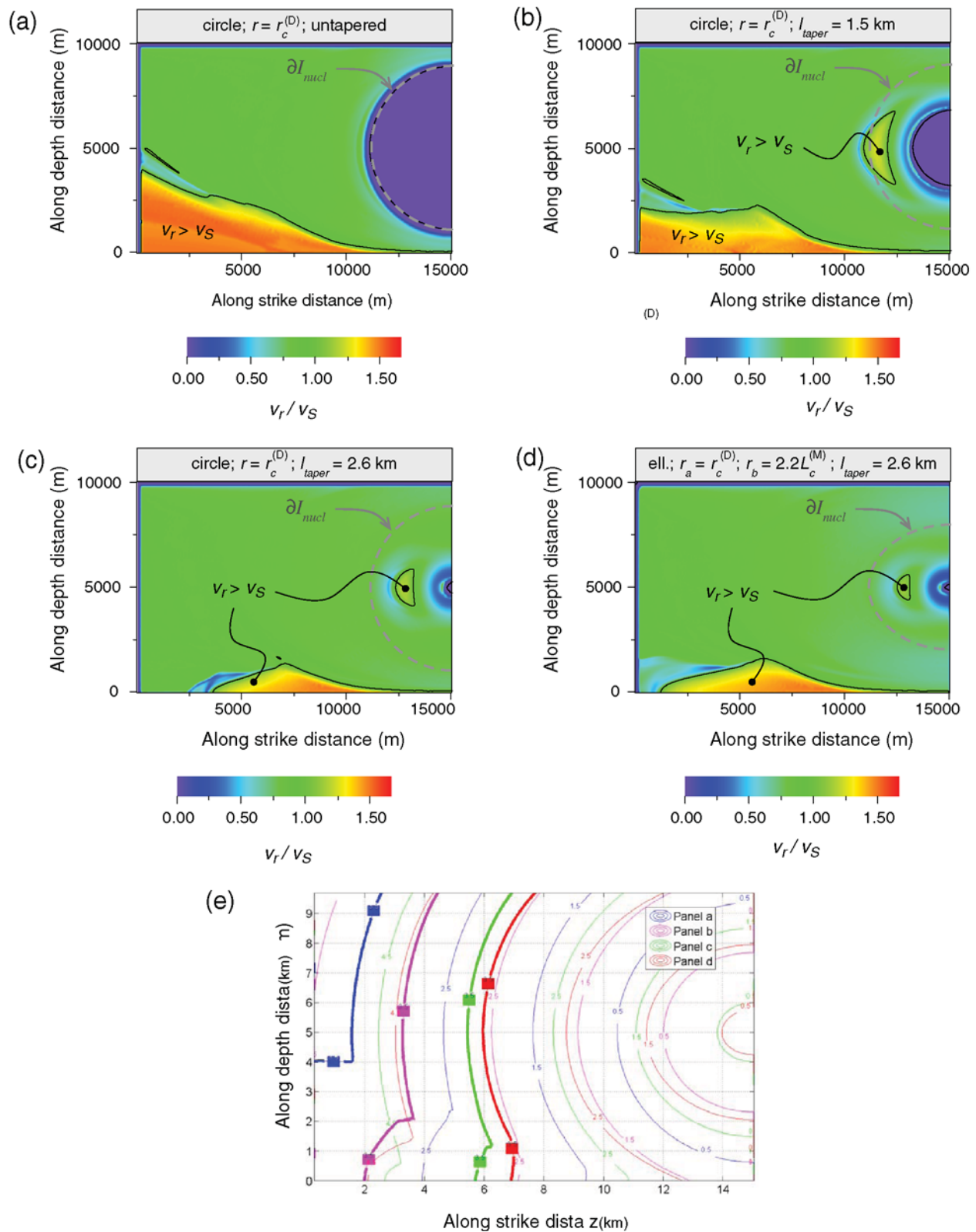
Figure A2. Effects of the nucleation parameters when an asperity in initial shear stress is imposed in the case of high strength fault. Ratios v_r/v_S when at $t=0$ are applied (a) a circular asperity of radius $r=r_c^{(D)}$; (b) a smoothed circular asperity with $r=r_c^{(D)}$ and $l_{taper}=1.5$ km; (c) a smoothed circular asperity with $r=r_c^{(D)}$ and $l_{taper}=2.6$ km; and (d) a smoothed elliptical asperity with $r_a=r_c^{(D)}$ and $r_b=r_c^{(D)}\frac{L_c^{(III)}}{L_c^{(II)}}$. The extension of I_{nucl} and the fault patches where v_r is locally supershear are indicated. (e) Comparison between resulting rupture times; the curves corresponding to 3.5 sec are displayed with thick lines.

Figure A3. Effects of the nucleation parameters when a perturbation in particle velocity is assumed in the case of high-strength fault. Ratio v_r/v_S when a perturbation to the particle velocity is applied at $t = 0$ within a fault patch parameterized by $l_1 = l_2 = r_c^{(D)}$ in the case of (a) $d_{nucl} = 20$ m and (b) $d_{nucl} = 40$ m. (c) Comparison between the resulting rupture times; the curves corresponding to 3.5 sec are displayed with thick lines.

just outside I_{nucl}. This behavior, which is in contrast with criterion (2), is more evident as d_{nucl} increases. Within the annular blue region enclosing I_{nucl}, the rupture velocity is highly oscillatory; this region is modulated by the value of d_{nucl} and in extreme cases ($d_{nucl} > 50$ m) inhibits the dynamic rupture propagation.

Istituto Nazionale di Geofisica e Vulcanologia
Sezione di Bologna, Italy Via Donato Creti, 12
40128 Bologna, Italy
bizzarri@bo.ingv.it